Cislunar Debris from Halo Object Breakups

Charles J. Wetterer[1], Christopher Craft[1], Jason, Baldwin[2], Micah Dilley[1], Paul Billings[1], John Gaebler[1], and Jill Bruer[3]
[1]*KBR*
[2]*Complex Futures*
[3]*Air Force Research Laboratory*

CONFERENCE PAPER

The increase in the utilization of cislunar space necessitates a better understanding of sustainability and the evolution and distribution of debris from cislunar orbits, whether from collisions, breakups, or satellite disposal. Possibilities include sublunar orbits (Earth-centered semi-major axes less than that of the Moon and eccentricities less than some specified limit), superlunar orbits (semi-major axes greater than that of the Moon and eccentricities less than the same limit), highly eccentric orbits (eccentricities greater than the specified limit but less than one), hyperbolic orbits (eccentricities greater than one), lunar orbits, Earth impacts, and Moon impacts. The proportions of debris in these categories will, in many cases, vary over time due to further interactions with the Moon. Current debris models, such as NASA's Orbital Debris Engineering Model (ORDEM), are designed for low-Earth orbit (LEO) and geosynchronous Earth orbit (GEO) and do not account for this type of debris nor model the debris environment in cislunar space. The added complexity of the orbital dynamics due to the influence of the Moon's gravity not only makes cislunar orbit determination and tracking of objects more difficult, but it also makes the potential debris environment more dynamic. To start investigating this dynamic environment, breakups in two different cislunar orbit families (the northern halo families about the $\mathscr{L}1$ and $\mathscr{L}2$ Lagrange points, termed "HN1" and "HN2") were simulated using NASA's General Mission Analysis Tool (GMAT) as the dynamics model and propagated forward in time for six months, and the resulting debris field distribution was examined as a function of time. Because this was a preliminary study to investigate the generic evolution of the resulting fragments, we simulated isotropic breakups with a characteristic breakup speed (while conserving total momentum) instead of using more sophisticated impact or explosion models based on satellite shapes, composition, and other details about the collision/explosion (e.g., NASA's Standard Satellite Breakup Model (SSBM)). We compared the resulting fragment distributions from these generic breakup events, both between orbit families and within each orbit family, and examined variations due to the timing of the breakup in each orbit and intensity of the breakup (as quantified by the average relative velocities between debris particles at the time of breakup). For example, the relative synodic phase of the object within the halo orbit will greatly influenced the fraction of particles that move into each of the defined orbit classes for the same progenitor orbit (e.g., for HN1 family orbits, more sublunar fragment orbits are produced when the progenitor is leading the Moon at time of breakup). Debris distribution variations as a function of the orbit's Jacobi Energy, proximity to Moon, Lyapunov stability characteristics, and proximity to Lagrange points were examined. The goal is to use these orbital characteristics to determine a measure of volatility related to a cislunar orbit's debris-creating potential.

1. INTRODUCTION

Our previous papers provide an overview of the expected photometric and astrometric measurements of objects in cislunar orbits [1], demonstrate the use of these observations to include passive RF to track objects in these orbits using estimation filters [2] [3], and explore the detection and characterization of impulsive maneuvers for an object in a cislunar orbit using similar estimation filters [4]. In this paper we examine the evolution of the distribution of particles in cislunar space that results from a breakup of an object in a cislunar halo orbit to start to understand the possible debris environment in this region. Whether from collisions, breakups or satellite disposal, the increased use of cislunar orbits will result in the accumulation of debris objects. Unlike breakups in low Earth orbit (LEO) or Geosynchronous Earth orbit (GEO) where debris is relatively confined to similar orbits as the progenitor object, cislunar breakups can distribute debris throughout the Earth-Moon system and into all orbital regimes to include Earth and Moon impacts or ejection from the Earth-Moon system entirely. How this debris evolves over time and whether any steady-state conditions are likely; which halo orbits contribute more or less to certain populations of debris; and dependencies on the location in the orbit or breakup velocities are the questions addressed in this paper.

Distribution A: Approved for public release; distribution is unlimited. Public Affairs release approval AFRL-2023-4014

2. BACKGROUND

Many of the periodic orbits in the circularly restricted three-body problem (CR3BP) (e.g., those emanating from the $\mathscr{L}1$ and $\mathscr{L}2$ Lagrange points) are unstable. These instabilities can be identified and characterized using classical Floquet analysis. Such an analysis is used in time-periodic systems (with a period of T) to find a T-periodic modal matrix $F(t)$ and a constant matrix J in Jordan normal form such that the periodic orbit's state transition matrix $\Phi(t,0)$ may be decomposed as

$$\Phi(t,0) = F(t)\,e^{Jt}\,F^{-1}(t) \tag{1}$$

This decomposition is most conveniently performed over one period using the monodromy matrix $\Phi(T,0)$, so that

$$\Phi(T,0) = F(0)e^{JT}F^{-1}(0) \tag{2}$$

And, assuming the system is posed in canonical coordinates and $F(0)$ is symplectic, the modal transformation matrix may then be propagated via

$$\frac{d}{dt}F(t) = A(t)\,F(t) - F(T)J \tag{3}$$

where $A(t)$ is the dynamics Jacobian. The diagonal elements of the matrix J are termed the Floquet (or Poincaré) exponents; in the problem of periodic orbits, two of these elements will be zero (corresponding to the degenerate modes), and the others will be either in complex-conjugate pairs (denoting oscillatory behavior) or positive/negative real pairs, denoting the unstable and stable modes, respectively.

The eigenvector in $F(t)$ associated with the unstable mode may be used to create a physical displacement which can then be propagated to yield a trajectory that maximally departs the reference trajectory. The collection of all trajectories formed from infinitesimal state displacements in this way (for all $t \in [0,T)$) constitutes a 2-dimensional invariant manifold called the "unstable manifold." A similar process using the stable mode eigenvector of $F(t)$, but propagating backwards in time, yields the so-called stable manifold. In the CR3BP, these manifolds are time-invariant geometric structures. An example of the stable and unstable manifolds for a northern $\mathscr{L}1$ halo orbit is shown in Fig. 1.

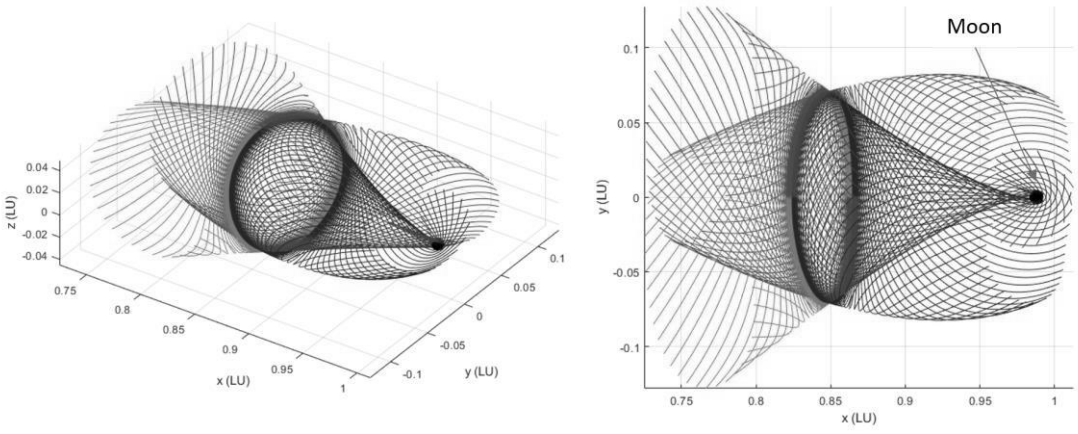

Fig. 1. Example stable (green) and unstable (red) manifolds for a northern $\mathscr{L}1$ halo orbit.

The modal matrix $F(t)$ may be interpreted as a transformation (to first order) between small displacements in the canonical coordinates (from the reference orbit) and the set of modal variables $\eta(t)$; that is, $\delta x(t) \approx F(t)\eta(t)$. Thus, we can characterize the motion of a trajectory "close" to the reference orbit (i.e., over relatively short periods of time) by treating the modal inverse $F^{-1}(t)$ as a projection of a physical displacement vector into the non-orthogonal modal basis.

As an example, consider the northern $\mathscr{L}1$ Halo orbit with an approximately 12.1-day period (labeled HN1-096). A portion of this orbit's unstable manifold is shown in red in Fig. 2**Error! Reference source not found.**; the interior branch of the unstable manifold (i.e., that which trends towards the moon) is colored dark red, while the exterior branch is shown in bright red. Consider a breakup occurring at a single point in the orbit, with each particle's Δv chosen from a normal distribution with a standard deviation in each direction of approximately 1 m/s. Trajectories of particles generated in this manner are shown in the figure as blue curves. As expected, the curves closely follow the shape of the unstable manifold.

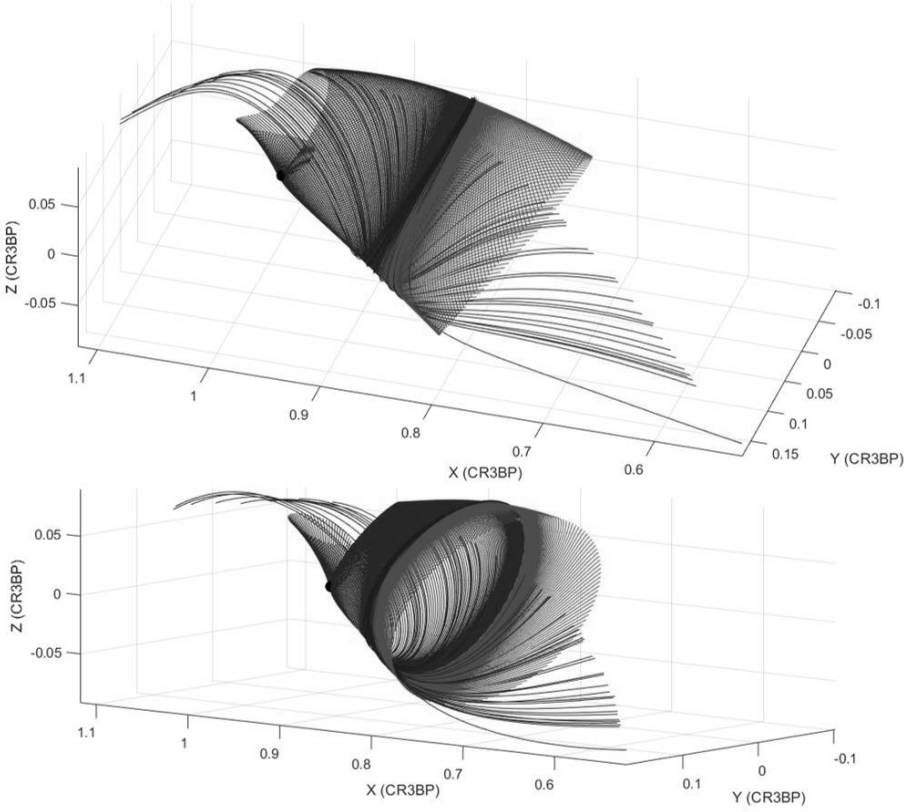

Fig. 2. Two views of sample trajectories (blue) of a 1-m/s breakup from an HN1-096 orbit after 10.5 days, shown with a portion of the orbit's unstable invariant manifold (red).

The inverse modal matrix $F^{-1}(t)$ at the breakup time is calculated, normalized, and then used to transform each particle's displacement $\delta x = [\mathbf{0} \quad \Delta v]^T$ into modal variables. Then, each particle's propagated distance from the reference orbit (after 10.5 days) is plotted as a function of the projection of the displacement into the unstable mode (see Fig. 3). The general behavior, for this propagation duration, shows nearly monotonic growth in each direction (positive and negative projections), meaning that this projection measure may be used as a proxy for instability of individual particles.

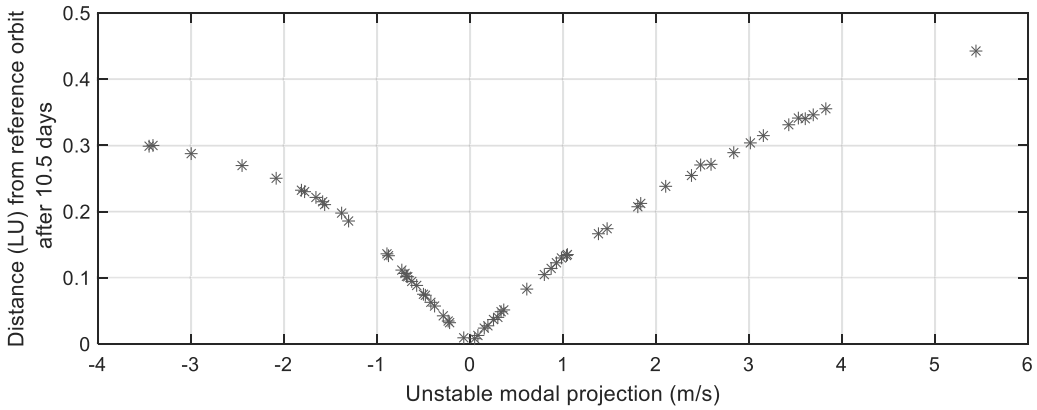

Fig. 3. Propagated distance of each breakup particle from the HN1-096 reference orbit as a function of the displacement's projection into the orbit's unstable mode at the breakup time.

However, as seen in the left side (negative projections) of Fig. 3, corresponding to the interior branch of the manifold, the relationship between the projection and the propagated distance begins to "fold" due to the deformation of the trajectories as they approach the Moon. Propagating for a longer time causes the left side of the plot to be increasingly non-monotonic, which indicates that the instability metric may be useful for stability comparison only for limited periods of time. This length of time will depend upon the period of the reference orbit, the orbit's proximity to the Moon or Earth, and the magnitude of its unstable Floquet exponent. These complex and chaotic interactions with the three-body gravitational field drive the need to resort to statistical techniques for long-term distributional trends, as detailed in the following sections.

It is of note that the gravitational perturbation from the Sun and the ellipticity of the Moon's orbit cause distinct changes in the shape of the unstable manifold (which is no longer invariant due to the addition of additional phase variables). Experiments in the Bicircular Restricted Four-body Model and the full-ephemeris model show that, for a breakup scenario, the near-monotonic relationship demonstrated in Fig. 3 qualitatively preserved, in general, in the presence of perturbative effects; this is due to the fact that the particles emanate from the same origin. When considering particles that start from different origins or at different times, the perturbative effects on the unstable manifold should be taken into account to determine relative instability; however, these scenarios are not considered further in the current work.

3. ORBITS AND BREAKUP SCENARIOS

We evaluated breakups in the northern portion of the halo families about the $\mathscr{L}1$ and $\mathscr{L}2$ Lagrange points. Specifically, six representative orbits were selected from the HN1 subset of the H1 periodic cislunar family (002, 096, 190, 284, 378, 472), and the HN2 periodic cislunar family (002, 104, 206, 308, 410, 512). Note that, similar to what was done in [1], periodic orbit families are represented by a discretization into 512 orbits. For the HN1 subset of the H1 family, this is between the L11 bifurcation point between the H1 and L1 families to the H11 bifurcation point between the H1 and W4W5 families. For the HN2 family, this is the entire family from the L21 bifurcation point between the HN2, L2 and HS2 families to the end (lunar impact). The details of the orbits are listed in Table 1. In these orbits, eight breakup times were used starting at the aposelene position and going $1/8^{th}$ of a synodic period in time from that point. Additionally, ten different characteristic breakup speeds, as measured by the root mean square (RMS) of the particle component speeds (logarithmically spaced from 10^{-4} km/s to 10^{-1} km/s) were used. The specific RMS speeds are (in m/s): 0.100, 0.215, 0.464, 1.000, 2.154, 4.642, 10.000, 21.544, 46.416, 100.000. The lower RMS speeds were chosen to include loss of control/satellite disposal possibilities while the upper RMS speeds are representative of fragment delta-v speeds from the NASA orbital debris breakup model [5]. Much larger speeds are possible from impacts, but the resulting debris gets distributed in much the same way, only faster. Finally, all breakup particles were given the same area-to-mass ratio (AMR=0.0109 m^2/kg). Fig. 4 displays these orbits with circled x's marking the aposelene position and x's marking the other breakup locations per orbit in the synodic frame. Two of the orbits label the positions with numbers from 0 to 7. The Moon's position is noted with a grey dot. Note that the orbits and characteristics in the figure and table are the idealized orbits in the CR3BP while the actual orbits used were ballistic orbits generated using full three-body dynamics and including solar radiation pressure that match as closely as possible the CR3BP orbits.

Table 1. CR3BP Orbit Characteristics

Name	Synodic Period (days)	Jacobi Constant
HN1-002	11.9273	3.17434
HN1-096	12.0850	3.12058
HN1-190	11.6434	3.02312
HN1-284	9.0620	2.99893
HN1-378	7.8925	3.00364
HN1-472	8.3636	2.98035
HN2-002	14.8492	3.15178
HN2-104	14.4256	3.10848
HN2-206	12.8558	3.03701
HN2-308	9.5898	3.01656
HN2-410	7.3360	3.03493
HN2-512	6.0453	3.05657

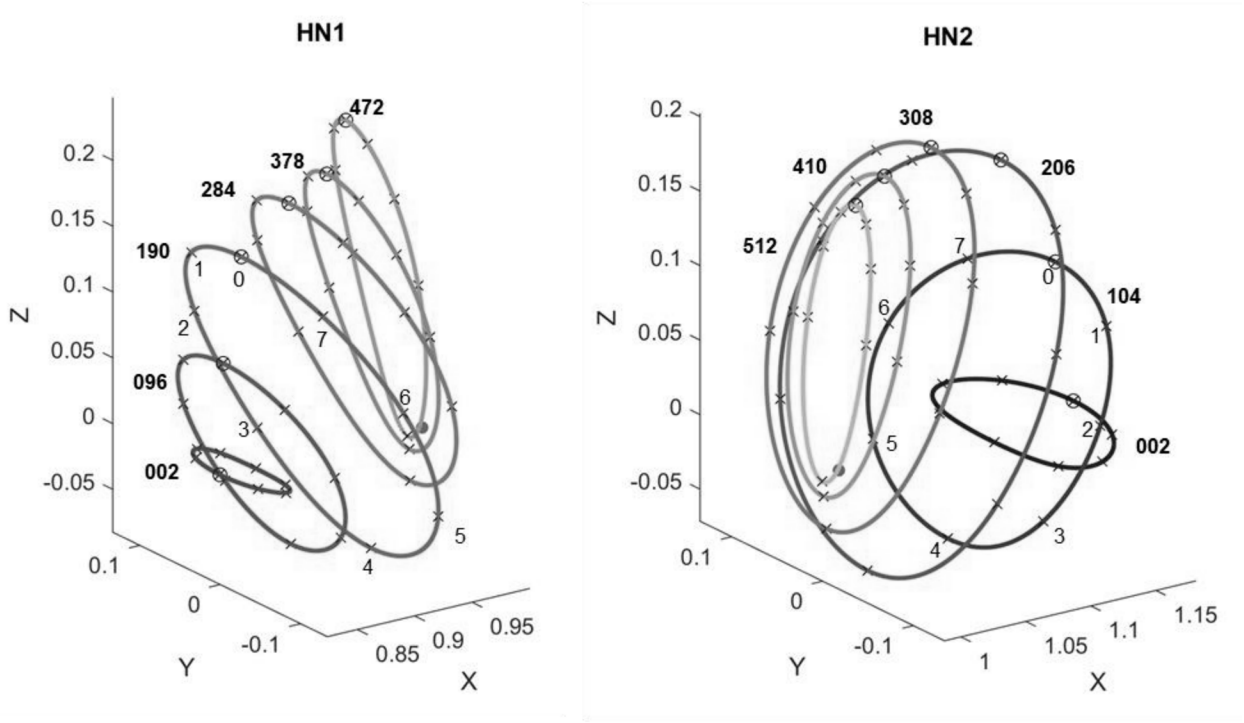

Fig. 4. HN1 and HN2 CR3BP orbits in synodic coordinates with breakup locations identified

All break-ups used the same velocity profile with 1024 breakup particles generated using a quasi-random distribution function based on the Sobol sequence [6] while also conserving linear momentum plus the original progenitor particle. Fig. 5 shows the distribution of particle velocity magnitudes for the 1024 breakup particles. The black line represents the same distribution for 1 million particles for comparison. Fig. 6 shows the distribution of particle velocities relative to the progenitor particle in synodic coordinates.

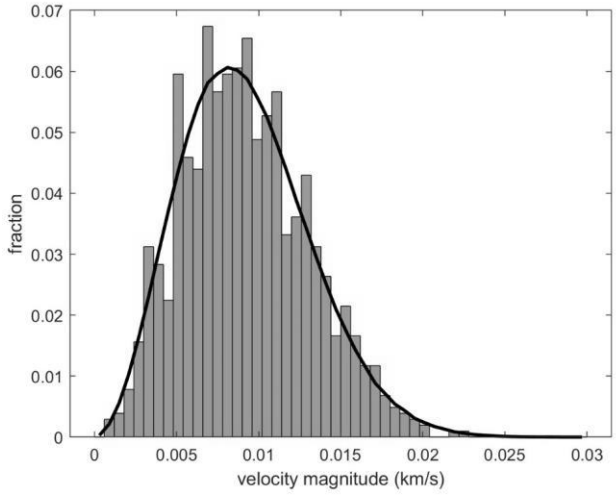

Fig. 5. Comparison of particle velocity magnitudes for 1024 particles (histogram) and 1 million particles (black line)

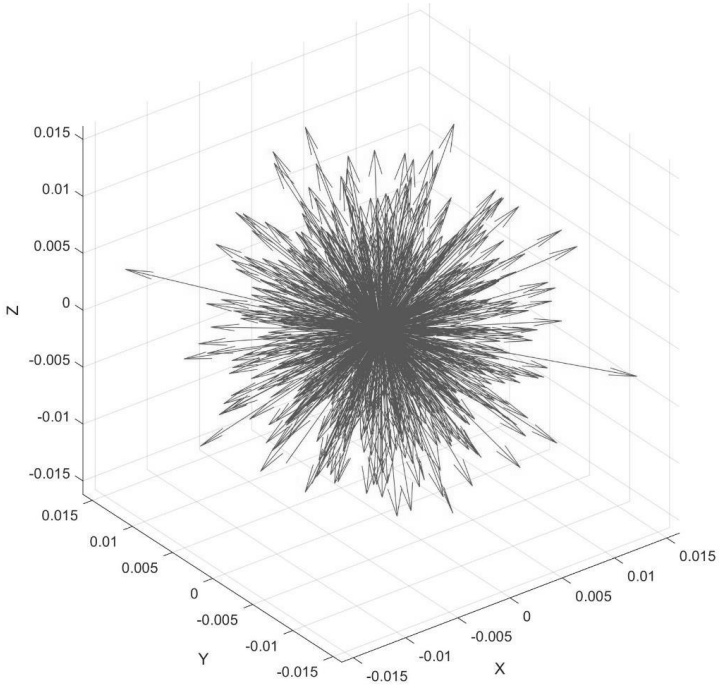

Fig. 6. Particle Velocity Distribution relative to the progenitor particle in synodic space. RMS = 10^{-2} km/s with axes in km/s.

All particles were propagated forward in time for 365 days using NASA's General Mission Analysis Tool (GMAT) as the dynamics model [7], which has the concept of a "primary" body utilizing a non-point mass gravitational field. To increase fidelity, the primary body during propagation was switched based on proximity to the Earth or Moon: Earth-centered (Sun and Moon point masses) using the EGM96.cof (20/20) Earth gravity model and Moon-centered (Sun and Earth point masses) using the grgm900c.cof (20/20) Moon gravity model. Impacts were attributed when the particle's distance from the Earth (RE) or Moon (RM) was under 6500 km or 1750 km respectively. The primary body was switched based on the particle's distance to the Moon: within 9990 km (Earth to Moon switch) or outside 10000 km (Moon to Earth switch). The dynamics model also included solar radiation pressure.

4. BREAKUP SCENARIO DEPENDENCIES

There are a total of 960 breakup scenarios compared (12 orbits × 8 breakup times × 10 RMS breakup speeds) in the following section as described in the previous section. To confirm this is representative of the range of possible breakups in these orbits, as well as the use of 1024 breakup particles, the gravity model used for the Moon, and a single area-to-mass ratio for all particles, we present finer delineated results for specific scenarios in this section showing the dependencies on the number of breakup objects, the Moon's gravity model, the area-to-mass ratio, the position of the breakup in the orbit, the RMS speed of the breakup particles, and the orbit number in the cislunar periodic family. The combinatorial explosion of these various parameters precludes exhaustive analysis but results are as expected in the cases examined.

To do this, we must first define the measures we used to compare the results between breakup scenarios. The first measure is by position of the resulting particles. Five positional regions were defined: Moon vicinity is distance from Moon (RM) < 100,000 km (beyond furthest halo orbit in set)), Sublunar is distance from Earth (RE) < 384,000 km (inside Moon's average distance and not in Moon's vicinity), Superlunar is RE > 384,000 km (outside Moon's average distance and not in Moon's vicinity), Outside is RE > 3,840,000 km (10× Superlunar or effectively ejected from Earth-Moon system), and Impacts (either Earth impact or Moon impact). The populations in each of these positional regions as a function of time over the course of the year were compared between scenarios. The second measure is the time required for at least 50% of the particles to leave the Moon vicinity region.

4.1. Number of breakup objects

Six test cases were run for the HN1-248 orbit with a breakup at the trailing point in the orbit (between position 5 and 6) and RMS speed of 10^{-2} km/s with 128, 256, 512, 1024, 2048, and 4096 breakup particles. For each case, the fraction of particles in each of the five positional regions were calculated for each day. Fig. 7 displays a comparison of these populations as a function of time for the 512 particle and 1024 particle cases.

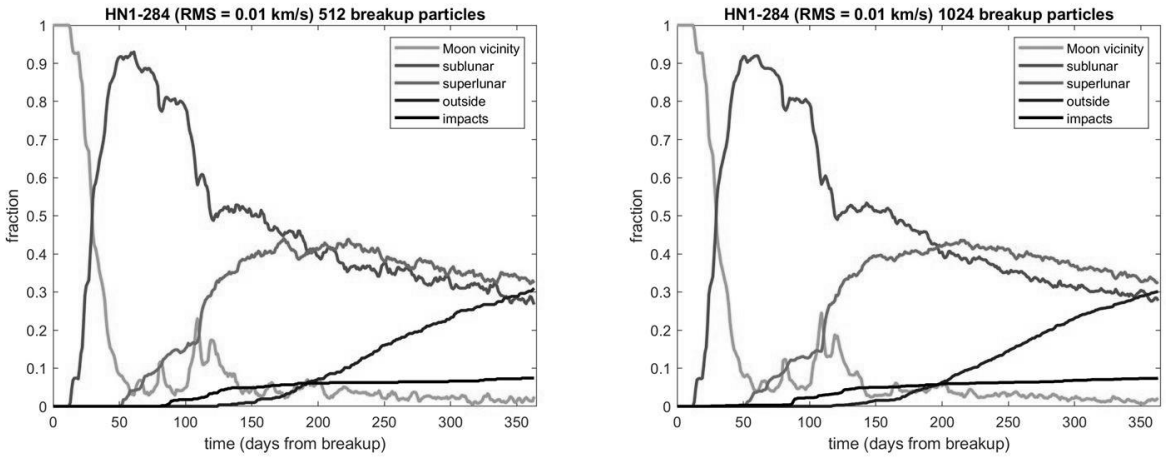

Fig. 7. Fraction in each population as a function of time for 512 particles (left) and 1024 particles (right) for HN1-284 orbit (trailing point and 10^{-2} km/s RMS speed). The general trends match with less noise for more particles.

Fig. 8 now plots the RMS values of the difference between the five lower particle cases to the 4096-particle case as a function of time and the average of the RMS value over all populations and times as a function of the number of particles. As expected, the more particles modeled in the breakup yields a closer match to the highest particle count case. 1024 particles per breakup was chosen as a compromise between the resulting uncertainty in the positional populations and computation time. The average RMS fractional difference is less than 1%.

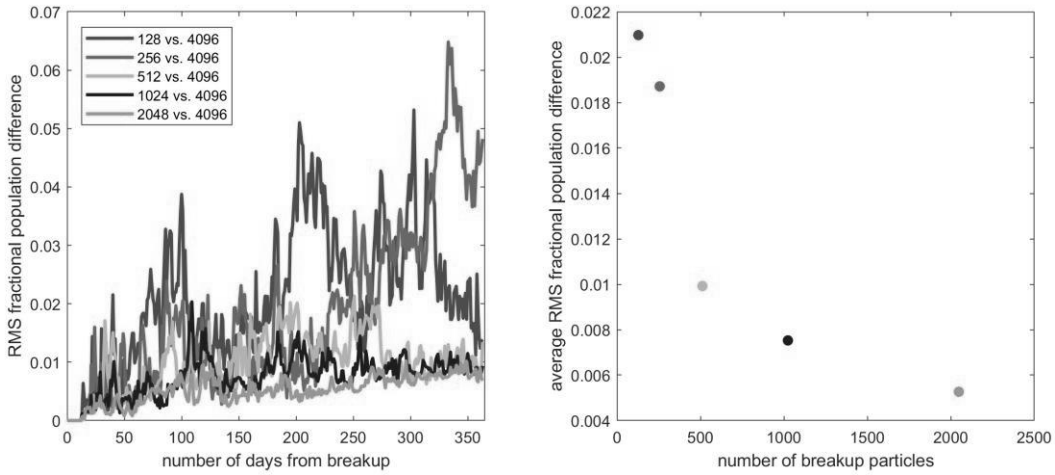

Fig. 8. RMS difference between populations and same population in 4096-particle breakup as function of time (left) and average value over all populations and all times (right) for HN1-284 orbit (trailing position and 10^{-2} km/s RMS). We selected 1024 particles (blue) as the "point of diminishing returns" balancing fidelity and computation demands.

4.2 Moon's gravity model

Three test cases were run for the HN1-002 orbit with a breakup at the trailing point (position 6) in the orbit and RMS speed of 10^{-2} km/s and AMR of 0.0109 m^2/kg for all particles. The first used the Earth-centered dynamics at all distances (treating the Moon as a point source always), the second used the LP165p.cof (20/20) gravity model for the Moon during Moon-centered dynamics, and the third used the grgm900c.cof (20/20) gravity model for the Moon during Moon-centered dynamics. Table 2 lists the populations for the different positional regions after 1-year of propagation after the breakup. Note that the impacts have been separated out into both Earth impacts and Moon impacts. Fig. 9 displays the difference between two of the breakup particles for the point-mass and grgm900c cases. Although the orbit of individual particles can vary greatly, the final statistics related to the positional regions is little changed. Since the computational burden of using the more complex and realistic lunar gravity model was minimal, the grgm900c model was adopted for this study.

Table 2. Populations (of 1025 particles) after 1-year for HN1-002 orbit (trailing point, 10^{-2} km/s RMS)

Lunar gravity model	Moon vicinity	Sublunar	Superlunar	Outside	Impact Earth	Impact Moon
point	18	278	43	152	9	525
LP165P	16	285	44	154	8	518
grgm900c	15	285	45	154	8	518

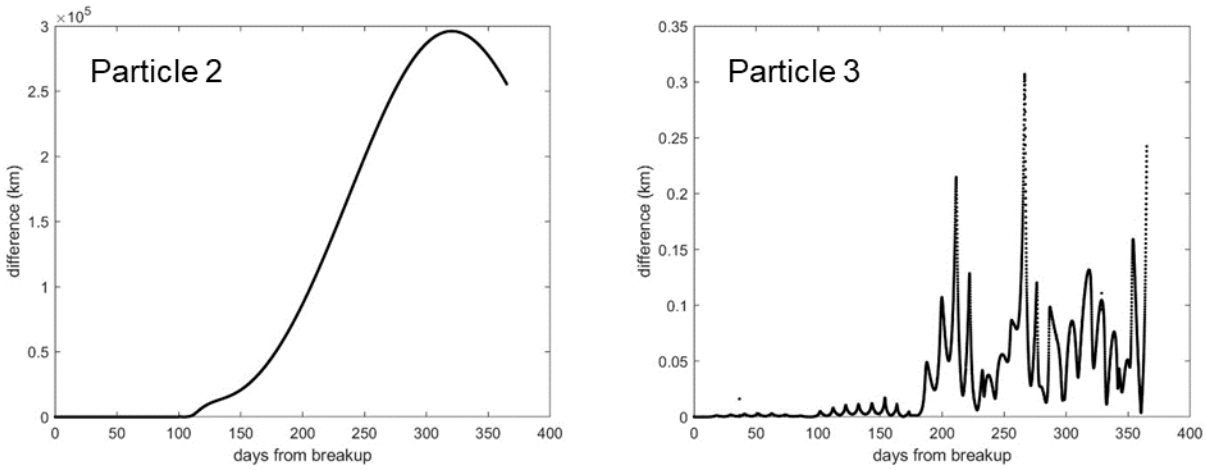

Fig. 9. Positional difference between point-mass and grgm900c lunar gravity models for two specific particles as function of time. The non-negligible difference of Particle 2 motivated the use of the more accurate model.

4.3 Area-to-mass ratio

One hundred test cases were run for the HN1-096 orbit with a breakup at the trailing point in the orbit (position 6) and RMS speed of 10^{-2} km/s with area-to-mass ratios ranging from 0.002 m^2/kg to 0.220 m^2/kg. Again, for each case, the fraction of particles in each of the five positional regions were calculated for each day. Fig. 10 displays the time in days when 50% of the particles are outside the Moon's vicinity and final positional populations as a function of area-to-mass ratio. The lines plotted in the positional plots are the associated mean values. Although the resulting orbits for individual particles are greatly affected by solar radiation pressure depending on the area-to-mass ratio, there is minimal dependence when comparing the variations in populations. Thus, a single value (0.0109 m^2/km) was chosen for all breakup particles in subsequent analyses.

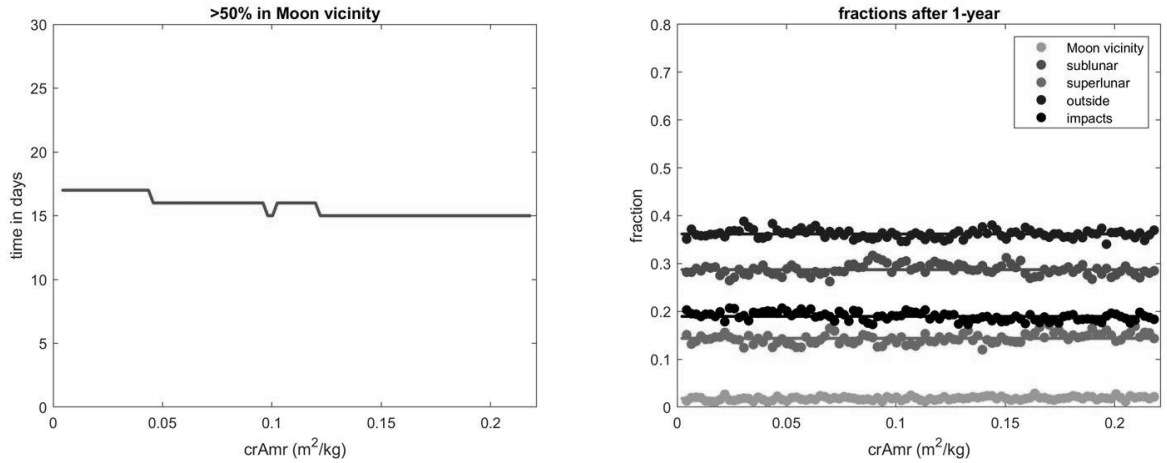

Fig. 10. Time in days for >50% of particles to leave Moon's vicinity (left) and final fractional populations after 1-year in each positional region (right) as function of area-to-mass-ratio for HN1-096 orbit (trailing position and 10^{-2} km/s RMS). Average over all values for each population also plotted as line. Little variation with crAmr was noted.

4.4 Position in orbit

One hundred test cases were run for the HN1-096 orbit with an RMS speed of 10^{-2} km/s with breakup time varied over a full synodic period starting at the trailing point in the orbit (position 6). Again, for each case, the fraction of particles in each of the five positional regions were calculated for each day. Fig. 11 displays the times to 50% outside Moon's vicinity and final positional populations as a function of orbit position (as measured by time). The solid lines are the moving mean trends for each population with significant dependency on orbit position present. Particularly note the anti-correlation between the number of impacts and the number that escape the Earth-Moon system (outside), and the anti-correlation between the number of impacts and the time >50% of the particles remain

in the Moon's vicinity. The latter is caused by a large number of impacts on the Moon soon after breakup when the debris front sweeps over the Moon and has not yet spread out considerably. This will be examined in more detail in the next section. Suffice for now is that the variations are relatively smooth with no dramatic changes over narrow ranges of position, and so choosing eight representative positions in the final comparisons is valid.

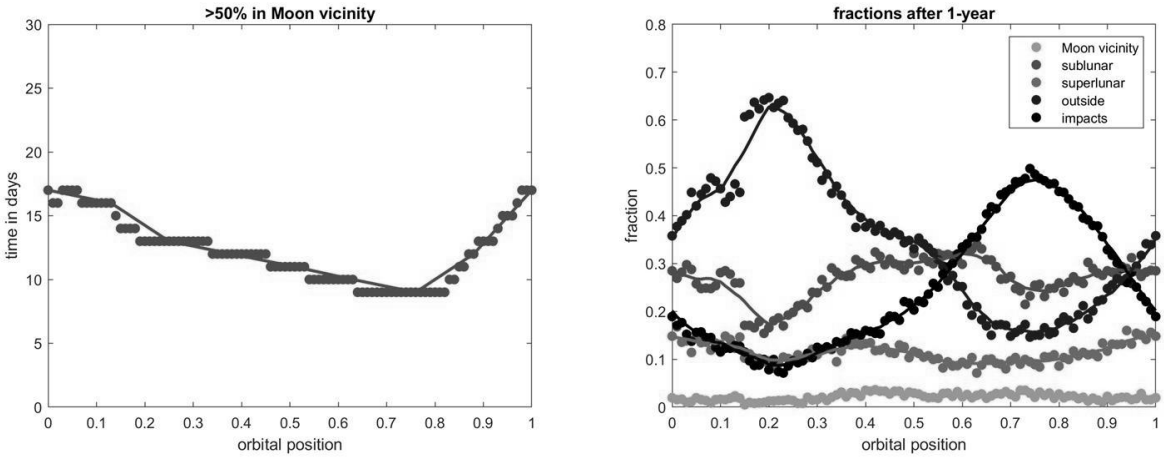

Fig. 11. Time in days for >50% of particles to leave Moon's vicinity (left) and final fractional populations after 1-year in each positional region (right) as function of position of the breakup in orbit for HN1-096 orbit (10^{-2} km/s RMS) where orbital position = 0 refers to the trailing position and other positions are measured by the fraction of the orbit's period. Moving mean over all values for each population plotted as lines. The smooth variation supports discretization into 8 representative positions for other analyses.

4.5 RMS speed of breakup

Sixty-one test cases were run for the HN1-096 orbit with a breakup at the trailing point and RMS speeds from 10^{-1} km/s to 10^{-4} km/s. Again, for each case, the fraction of particles in each of the five positional regions were calculated for each day. Fig. 12 displays the times to 50% outside Moon's vicinity and final positional populations as a function of RMS speed. The solid lines are the moving mean trends for each population. The anti-correlation between impacts and particles ejected from the Earth-Moon system is evident as before, but again the variations are smooth with no dramatic changes over narrow ranges of RMS speed, and so the choice of ten representative RMS speeds in the final comparisons seems valid. The anti-correlation between the impacts and the time >50% of the particles remain in the Moon's vicinity is evident for higher breakup RMS values, but not for lower RMS values. Again, for higher RMS values, there are a large number of impacts on the Moon soon after breakup when the debris front sweeps over the Moon and has not yet spread out considerably. For lower RMS values, the particles have not yet spread out enough when the debris front sweeps over the Moon the first time, but after a full synodic period (~16 days), a similar situation occurs resulting in a large number of impacts on the Moon.

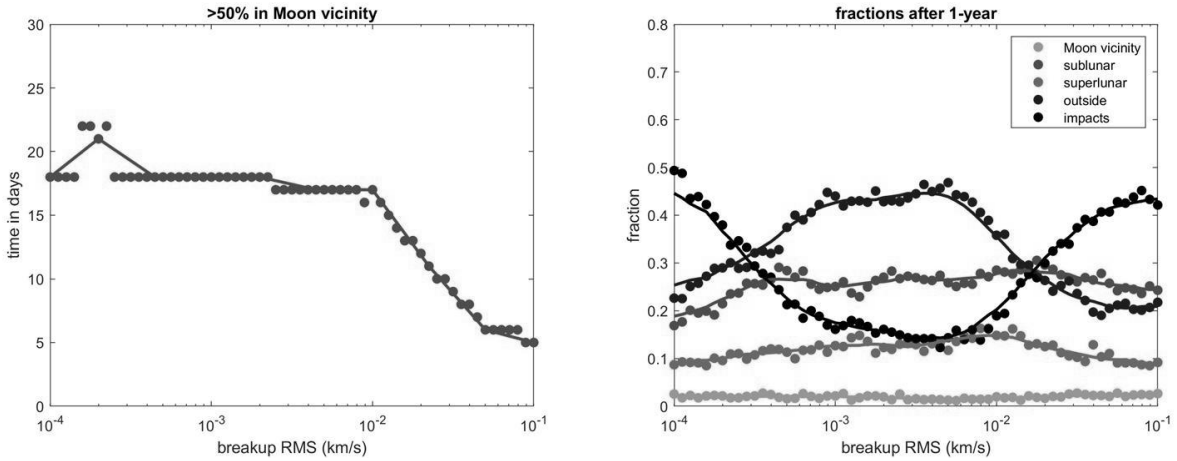

Fig. 12. Time in days for >50% of particles to leave Moon's vicinity (left) and final fractional populations after 1-year in each positional region (right) as function of RMS speed of the breakup for HN1-096 orbit (trailing position). Moving mean over all values for each population plotted as lines. The smooth variation supports discretization into 10 representative breakup speeds for other analyses.

4.6 Orbit number

Finally, five hundred nine test cases were run across most of the HN1 orbit family with breakups at the trailing point and RMS speed of 10^{-2} km/s. Note that, for orbit numbers greater than 490, the progenitor object's orbit actually intersects the Moon's surface. Even disregarding the possibility of impact, progenitor orbits for the three final cases in the family (orbits 510, 511, and 512) did not converge on a satisfactory solution and were not included in this analysis. As in the previous analyses, the fraction of particles in each of the five positional regions were calculated for each day. Fig. 13 displays the times to 50% outside Moon's vicinity and final positional populations as a function of orbit number (recall that orbit number 1 is close to the L11 bifurcation point between the H1 and L1 families while orbit number 512 is close to the H11 bifurcation point between the H1 and W4W5 families). The anti-correlation between impacts and particles ejected from the Earth-Moon system is evident as before, but again the variations are smooth with no dramatic changes over small changes in orbit number, and so choosing six representative orbits in the final comparisons is reasonable.

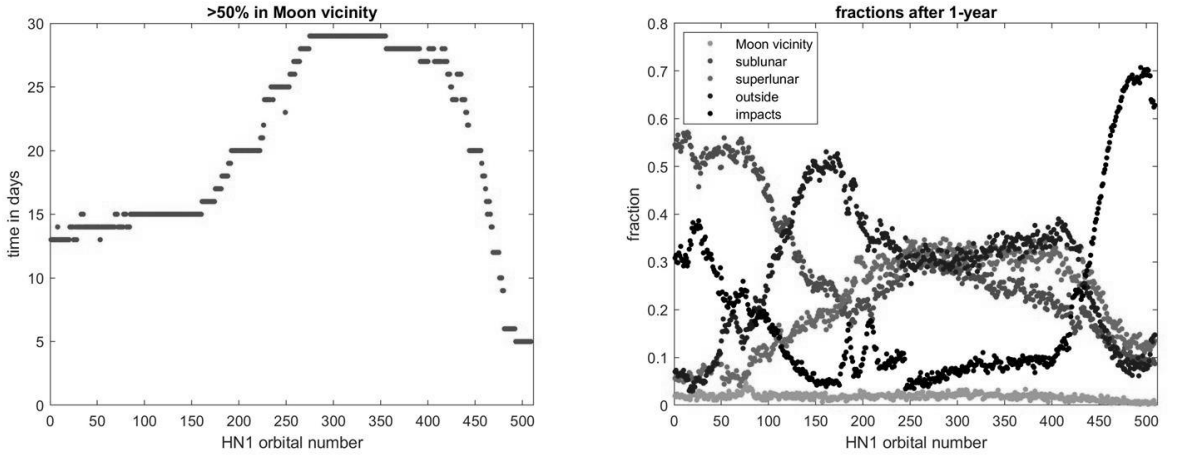

Fig. 13. Time in days for >50% of particles to leave Moon's vicinity (left) and final fractional populations after 1-year in each positional region (right) as function of orbit number for HN1 family (trailing position and 10^{-2} km/s RMS). Moving mean over all values for each population plotted as lines. The smooth variation supports discretization into 6 representative orbits per family for other analyses.

5. ANALYSIS

A total of 960 breakup scenarios (12 orbits × 8 breakup times × 10 RMS breakup speeds) representative of the variety of possible breakups in a cislunar halo orbit are compared. There are two key points we present. First,

cislunar breakups in halo orbits lead to debris in all orbit regimes. This is a stark contrast to GEO and LEO where breakups only contaminate similar orbits with the progenitor orbit. Second, the progenitor orbit and associated characteristics of the trajectories along the orbit's unstable manifold determine the divergence rate and resulting debris populations. Specifically, cislunar breakup particles are initially stretched out in directions associated with the orbit's unstable manifold. The speed at which particles leave the Moon's vicinity is related to "stability" of the progenitor orbit (i.e. unstable mode Floquet exponent) with longer times for more stable orbits. The resulting populations are determined by this combined with other orbital characteristics. For example, HN1 orbits lead to higher population of debris in sublunar than HN2 orbits, although interestingly both have nearly the same sub-GEO densities when debris reaches this region.

Fig. 14 shows the density of breakup particles as a function of geocentric distance for the first four months after breakup averaging over all breakup locations and speeds for a given orbit. The density is scaled by assuming a total of 10^9 particles in a single breakup. The vertical dashed line at about 10^{-1} Earth-Moon distances is GEO while the lower limit of the graphs is a high LEO orbit. Over time, the particle distribution contaminates all orbital regimes for all orbits with HN1 orbits (warmer colors) having higher sublunar densities than HN2 orbits (cooler colors) and vice versa for superlunar densities.

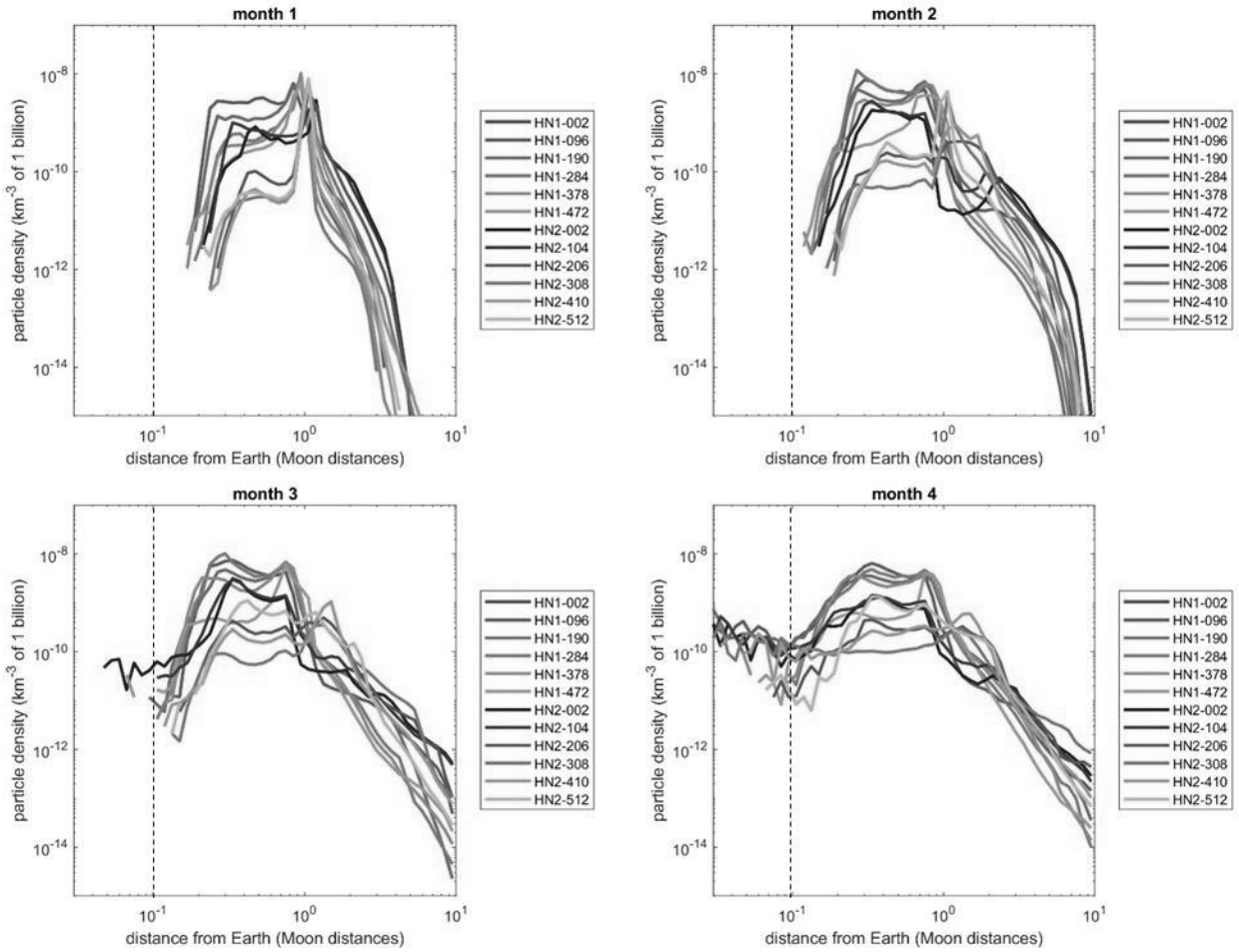

Fig. 14. Particle density from 10^9 particle breakup as function of distance (in Earth-Moon distances) for first four months after breakup by orbit averaged over all breakup positions and RMS breakup velocities

Fig. 15 plots the distribution of the HN1-002 breakup particles in synodic coordinates for two different RMS breakup speeds at two different times after breakup. Evident is how the distribution of breakup particles is stretched out in the preferential direction over time as defined by the unstable manifold. The effect is more noticeable for lower RMS breakup velocities as can be seen by comparing the RMS = 10^{-1} km/s to the RMS = 10^{-4} km/s plots. Also note how the smaller the RMS breakup speed, the longer it takes to leave the vicinity of the breakup, as would be

expected. This is why some orbits exhibit a large number of impacts as the particle front on the unstable manifold sweeps through the Moon soon after the breakup, as highlighted in the previous section.

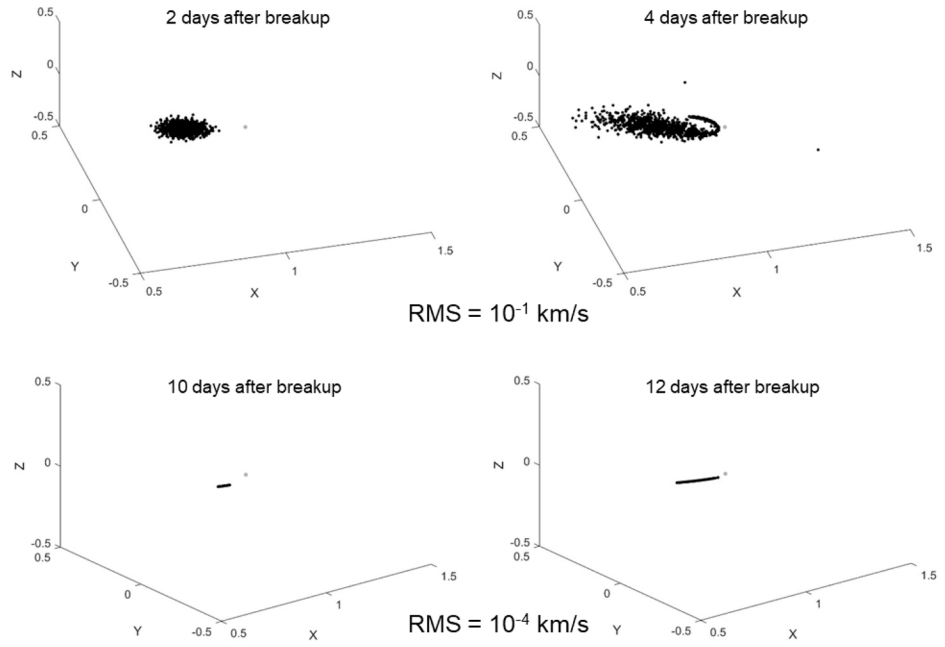

Fig. 15. Synodic distribution of breakup particles (black) about the Moon (gray) for two different RMS breakup speeds (top and bottom) and two different times after breakup (left and right). The unstable manifold dictates the direction of stretching.

In addition to the RMS breakup speed, the orbit's stability – measured by the unstable mode Floquet exponent – also plays a factor in the divergence rate. Fig. 16 plots the number of days it takes for 50% of the particles to leave the lunar vicinity (defined as 100,000 km from the Moon's center) as a function of orbit number averaged over all breakup locations with HN1 orbits plotted on the left-hand graph and HN2 orbits plotted on the right. The orbit identifiers (the independent axes) are plotted such that the $\mathscr{L}1$ Lagrange point is on the left side, the $\mathscr{L}2$ Lagrange point is on the right side and the Moon is in the middle between the plots. Generally, HN2 have longer times than HN1 for comparable RMS breakup speeds, and higher orbit numbers for both have longer times. One exception to this is for HN1 higher orbit numbers where there are more impacts due to the closer periselene values, and this reduces the time as the number of impacts soon after breakup add up. Fig. 17 plots the same as a function of the unstable mode Floquet exponent for two specific RMS breakup speeds. In this case it is the orbits with lower unstable mode Floquet exponents (more stable) that have longer times where again those with closer periselene values (and associated higher rate of impacts because of this) are off the general trend.

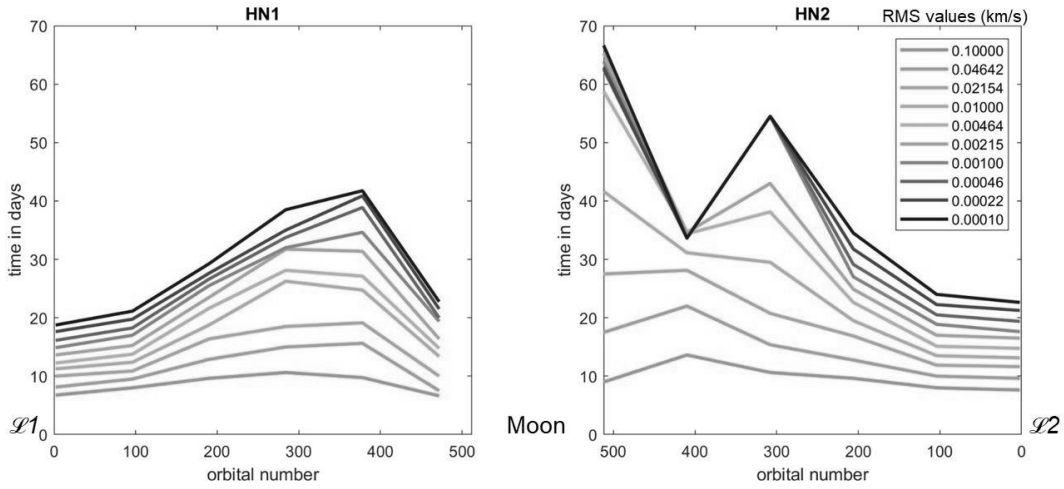

Fig. 16. Time in days for 50% of breakup particles to leave lunar vicinity (10,000 km from Moon's center) as function of orbit (HN1 orbits on left plotted left to right from orbits closest to $\mathscr{L}1$ Lagrange point to orbits closest to Moon, and HN2 orbits on right plotted right to left from orbits closest to $\mathscr{L}2$ Lagrange point to orbits closest to Moon, averaged over all breakup positions) and RMS breakup speed. Orbits nearer the moon take longer to leave the vicinity, with a decrease in time due to impacts.

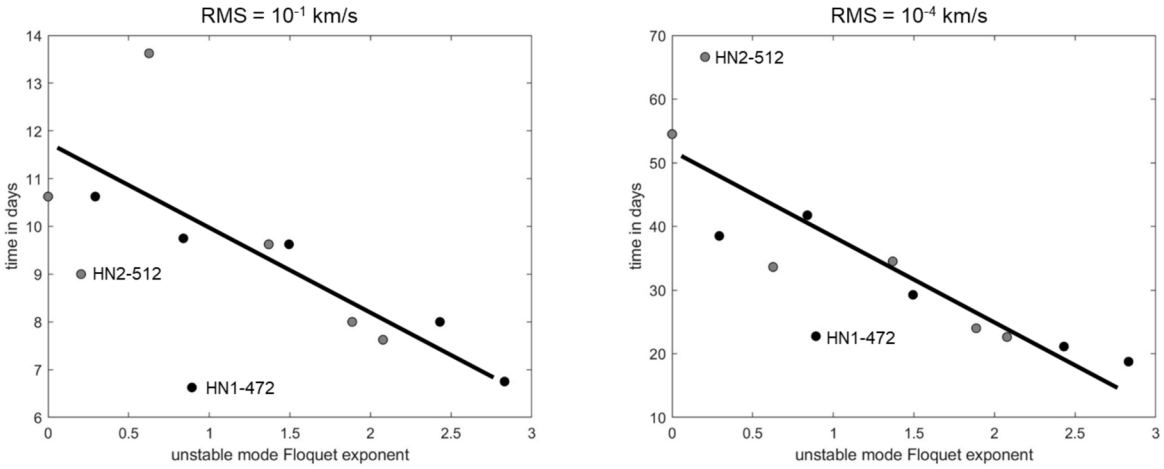

Fig. 17. Time in days for 50% of breakup particles to leave lunar vicinity (10000 km from Moon's center) as function of unstable mode Floquet exponent (HN1 orbits black dots and HN2 orbits gray dots averaged over all breakup positions) and two different RMS breakup speeds (left and right) with general trend highlighted. Higher number orbits where impacts due to low periselene values are labeled. As expected, lower Floquet exponents are more stable with particles remaining in the vicinity longer.

Fig. 18 plots population as a function of time for four specific cases corresponding to having the maximum number of particles in a particular population 1-year after the breakup. These correspond to 61% sublunar (for HN1-002 (RMS = 0.01 km/s) starting at position 0), 82% superlunar (for HN2-410 (RMS = 0.0001 km/s) starting at position 7), 100% outside (for HN2-308 (RMS = 0.0001 km/s) for all starting positions), and 71% impacts (for HN1-002 (RMS = 0.0002 km/s) starting at position 0). This is presented to underscore how breakups in cislunar halo orbits can lead to debris populations in a wide variety of orbital regimes that persist over time.

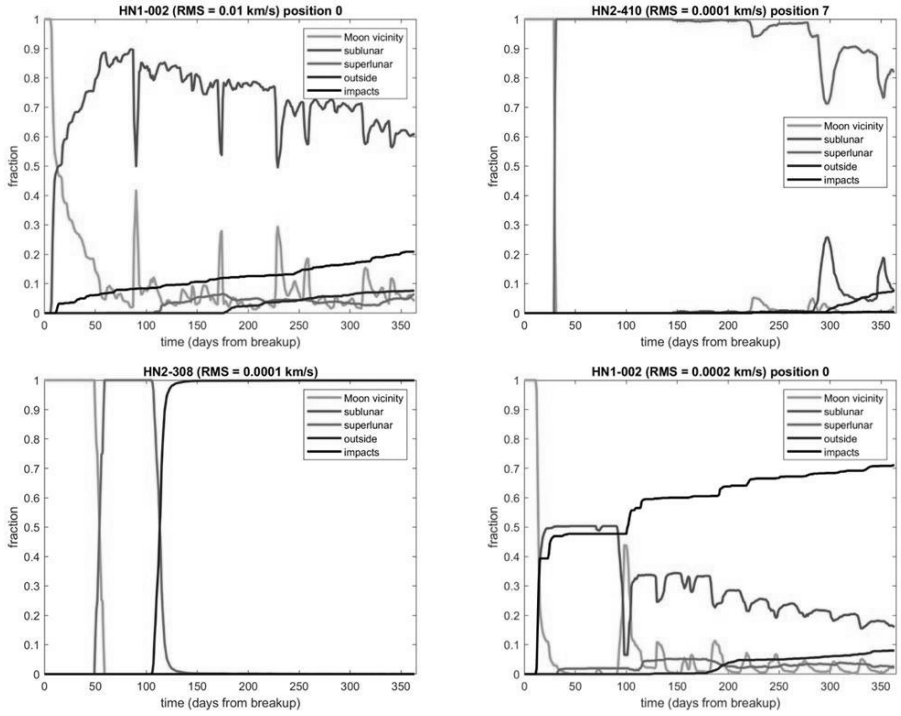

Fig. 18. Fractions of debris particles in various populations as function of time for four specific cases. Largest sublunar after one year (upper left), largest superlunar after one year (upper right), largest outside (ejected from Earth-Moon system) after one year (lower left) and largest number of impacts after one year (lower right).

Finally, it should also be noted that ejection from the Earth-Moon system (i.e. the "outside" population) does not mean these debris objects will permanently remain outside the Earth-Moon system. Recent significant examples of a man-made object which entered a Sun-centered orbit only to later be recaptured for a time by the Earth-Moon system are the Apollo 12 S-IVB rocket body [8] and Surveyor 2 Centaur upper stage [9]. As such, the Sun-centered orbital elements for the outside debris populations for six select orbits were calculated and propagated forward 28 years to examine their evolution over time. Fig. 19 plots the distribution of eccentricities, inclinations, and semi-major axes for all the resulting orbits as well as the estimated return time (as calculated by $|T/(T-1)|$ where $T = \mathrm{sqrt}(a_{AU}^3)$). It was discovered that approximately 14% of the debris objects are "recaptured" by the Earth-Moon system (as defined by the distance to the Earth becoming less than 10× the Earth-Moon distance) at each successive revisit ranging from fly-bys to Earth or Moon impacts. As such, given a long enough time, all cislunar debris objects will eventually return. Fig. 20 plots a sample of debris distance from Earth as a function of time for four representative cases.

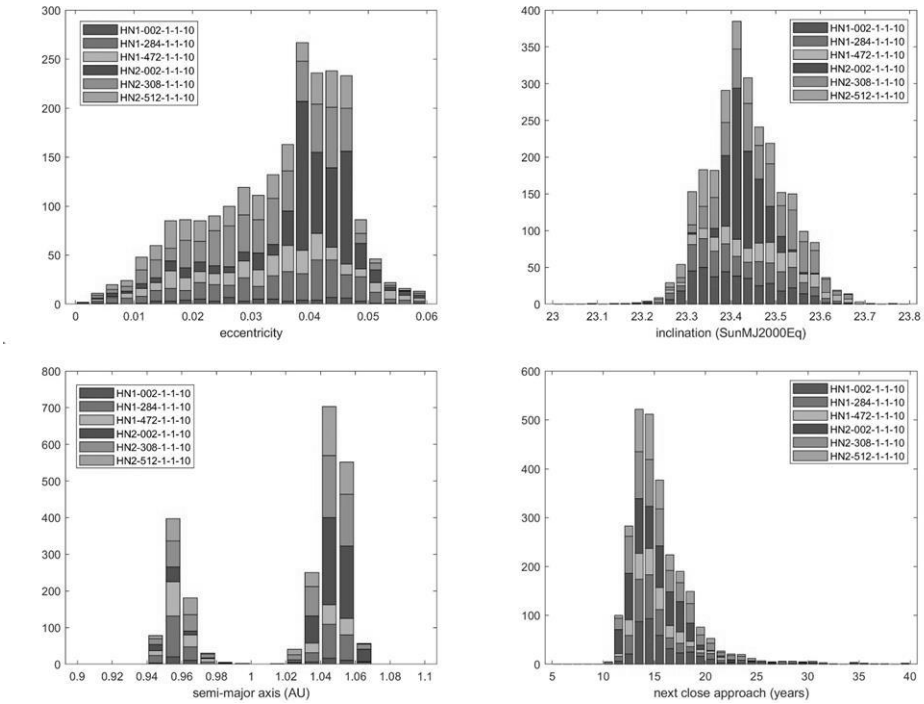

Fig. 19. Sun-centered orbital elements (eccentricity, inclination, semi-major axis) of 2297 debris objects from six representative orbits. Next close approach calculated using $|T/(T-1)|$ where $T = \mathrm{sqrt}(a_{AU}^3)$.

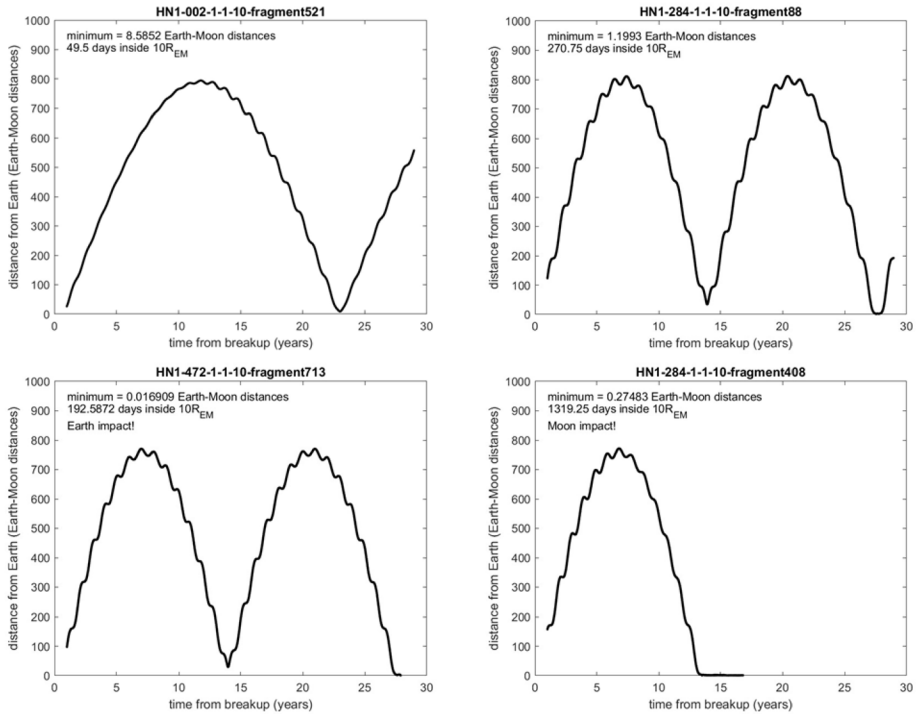

Fig. 20. Distance of debris particle from Earth (in Earth-Moon distances) as function of time for four representative cases: 50-day "fly-by" on first revisit (upper left), 271-day recapture on second revisit (upper right), Earth impact after 193-day recapture on second revisit (lower left), and Moon impact after 3.6-year recapture on first revisit (lower right)

6. SUMMARY

Cislunar breakups in halo orbits generally lead to a debris cloud that contaminates all orbit regimes regardless of the type of halo orbit, the location of the breakup in the orbit, and the speed of the debris particles. This is unlike other orbit regimes such as GEO and below where debris from a breakup, particularly with lower speeds, tends to stay fairly close to the progenitor object's orbit. The resulting evolution of the various debris populations (e.g. sublunar vs. superlunar) are tied back to the particular progenitor orbit, specifically the directions and characteristics of the trajectories along the orbit's unstable manifold.

7. REFERENCES

[1] C. Chow, C. Wetterer, K. Hill, C. Gilbert, D. Buehler and J. Frith, "Cislunar Periodic Orbit Families and Expected Observational Features.," in *The Advanced Maui Optical and Space Surveillance Technologies (AMOS) Conference, Maui, HI, September 15-18*, 2020.

[2] C. Chow, C. Wetterer, J. Baldwin, M. Dilley, K. Hill, P. Billings and J. Frith, "Cislunar Orbit Determination Behavior: Processing Observations of Periodic Orbits with Gaussian Mixture Model Estimation Filters," in *The Advanced Maui Optical and Space Surveillance Technologies (AMOS) Conference, Maui, HI, September 14-17*, 2021.

[3] C. Chow, J. Baldwin, C. Wetterer, M. Dilley, K. Hill, P. Billings, C. Craft and J. and Frith, "Cislunar Orbit Determination: Improvements in Uncertainty Realism and Data Fusion," in *Advanced Maui Optical and Space Surveillance Technologies (AMOS) Conference, Maui, HI, September 27-30*, 2022.

[4] C. Wetterer, C. Chow, J. Baldwin, M. Dilley, K. Hill, H. Montell-Weiland, P. Billings, C. Craft and J. and Frith, "Cislunar Maneuver Detection and Classification," in *Advanced Maui Optical and Space Surveillance Technologies (AMOS) Conference, Maui, HI, September 27-30*, 2022.

[5] A. Manis, M. Matney, A. Vavrin, J. Seago, D. Gates, P. Anz-meador, T. Kennedy, H. Cowardin and Y. Xu, "NASA Orbital Debris Engineering Model (ORDEM) 3.1 Model Process," NASA Technical Report, 2022.

[6] I. Sobol, *USSR Comput. Maths. Math. Phys.,* vol. 7, pp. 86-112, 1967.

[7] GMAT Development Team, "User's Guide," 2020.

[8] K. Jorgensen, A. Rivkin, R. Binzel, R. Whitely, C. Hergenrother, P. Chodas, S. Chesley and F. Vilas, "Observations of J002E3: Possible Discovery of an Apollo Rocket Body," *Bulletin of the American Astronomical Society,* vol. 35, no. 981, 2003.

[9] V. e. a. Reddy, "Challenges in Differentiating NEOs and Rocket Bodies: 2020 SO Study," in *7th IAA Planetary Defense Conference*, Vienna, Austria, 26-30 April 2021.